

Structure and rovibrational analysis of the $[\text{O}_2(^1\Delta_g)_{v=0}]_2 \leftarrow [\text{O}_2(^3\Sigma_g^-)_{v=0}]_2$ transition of the O_2 dimer

Ludovic Biennier,^{a)} Daniele Romanini, Alexander Kachanov, and Alain Campargue^{b)}
*Laboratoire de Spectrométrie Physique (CNRS UMR 5588), Université J. Fourier de Grenoble,
 B.P. 87, 38402 Saint Martin d'Hères Cedex, France*

Béatrice Busserly-Honvault
*Laboratoire de Physique des Atomes, Lasers, Molécules et Surfaces (CNRS UMR 6627),
 Université de Rennes I, Bât. 11B, Campus de Beaulieu, 35042 Rennes Cedex, France*

Roger Bacis
*Laboratoire de Spectrométrie Ionique et Moléculaire (CNRS UMR 5579), Université Lyon I,
 Bât. 205, Campus de la Doua, 43 bd du 11 Novembre 1918, 69622 Villeurbanne Cedex, France*

(Received 19 October 1999; accepted 19 January 2000)

The rotationally resolved absorption spectrum of the O_2 dimer involving the $[\text{O}_2(^1\Delta_g)_{v=0}]_2 \leftarrow [\text{O}_2(^3\Sigma_g^-)_{v=0}]_2$ transition has been recorded near 632.6 nm by continuous wave Cavity Ring Down Spectroscopy in a supersonic slit jet expansion of pure O_2 . A quadratic dependence of the absorption in the jet versus the stagnation pressure is observed. A rotational temperature of 12 K is derived from the $(\text{O}_2)_2$ rotational analysis. The high spectral resolution of the CW-CRDS measurements limited by the residual Doppler broadening in the jet and the low rotational temperature allow the first rotational analysis in this open-shell complex. The same spectrum was also recorded by Intracavity Laser Absorption Spectroscopy and the comparison of the performances of the two methods is discussed. Among more than 600 lines measured between 15 800 and 15 860 cm^{-1} from the CW-CRDS spectrum, 40 were assigned to the $^R P_0$, $^R Q_0$, and $^R R_0$ branches of two subbands associated with $B_1^- \leftarrow A_1^+$ and $A_1^+ \leftarrow B_1^-$ transitions between the ground and excited rovibrational levels, labeled following the G_{16} permutation inversion representation. Forty five lines were assigned to $^P P_2$, $^P Q_2$, and $^P R_2$ branches of two subbands associated with $B_1^- \leftarrow A_1^+$ and $A_1^+ \leftarrow B_1^-$ transitions. The subbands centered at 15 808.401(49) [$A_1^+ \leftarrow B_1^-$] and 15 813.134(37) cm^{-1} [$B_1^- \leftarrow A_1^+$] for those arising from $K=0$, and at 15 812.656(20) [$A_1^+ \leftarrow B_1^-$] and 15 818.277(35) [$B_1^- \leftarrow A_1^+$] when arising from $K=2$, are analyzed considering $(\text{O}_2)_2$ as a slightly asymmetric prolate top. The rotational analysis of the two $K=0$ subbands leads to very close values of the effective rotational constant, $B_p = (B+C)/2$, for both A_1^+ and B_1^- levels: 0.095 cm^{-1} for the $[\text{O}_2(^3\Sigma_g^-)_{v=0}]_2$ lower states and 0.063 cm^{-1} for the $[\text{O}_2(^1\Delta_g)_{v=0}]_2$ excited states, in close agreement with theoretical values. The H geometry is confirmed as the most stable for the ground electronic singlet state. A distance between the two monomers of 6.1 a_0 and 7.5 a_0 is derived for the ground and excited singlet states. Similar results are obtained from the two $K=2$ subbands. A vibrational assignment is given for the two rotationally analyzed subbands ($K=0$) and proposed for the main features of the whole band. © 2000 American Institute of Physics. [S0021-9606(00)01614-7]

I. INTRODUCTION

The development of powerful high resolution optical techniques associated with supersonic jets has given a new insight on weakly bound molecular species relevant to atmospheric physics and chemistry, such as $(\text{CO}_2)_2$,¹⁻³ $(\text{H}_2\text{O})_2$,^{4,5} or the oxygen dimer.⁶ The importance of the oxygen dimer has been recently highlighted by kinetic studies relative to the ozone cycle. Wodkte *et al.*⁷ showed that the oxygen dimer may be involved in a new production channel of ozone in the stratosphere through the mechanism $[\text{O}_2(^3\Sigma_g^-)_{v \geq 26} - \text{O}_2(^3\Sigma_g^-)_{v=0}] \rightleftharpoons \text{O}_3(X^1A_1) + \text{O}(^3P)$. This observation

may help to address the ‘‘ozone deficit problem’’ and numerous theoretical (see Refs. 8, 9 and references therein) and experimental studies¹⁰⁻¹⁴ relative to this chemical equilibrium have been carried out (see the recent results and discussion on this problem in Ref. 15).

According to an estimation of Ref. 16, O_2 complexes absorb about 1.5×10^{-3} of the total solar energy reaching the earth atmosphere. In particular, they may affect ozone concentration measurements by scattering of light as some collision-induced absorption bands of $(\text{O}_2)_2$ overlap the Chappuis and Hartley bands of ozone. The recent observation by the Hubble Space Telescope of visible absorption bands associated with condensed phase spectra of oxygen on Jupiter’s satellite, Ganymede, has given a clue to the mode of production and stability of oxygen through its latitudinal

^{a)}Electronic mail: Ludovic.Biennier@ujf-grenoble.fr

^{b)}Electronic mail: Alain.Campargue@ujf-grenoble.fr

distribution.¹⁷ In the chemical lasers research field, Yoshida *et al.*¹⁸ observed an unexpected red fluorescence in a Chemical Oxygen Iodine Laser and demonstrated the possibility to get the inversion population of an excited metastable state of $(\text{O}_2)_2$, similarly to excimer lasers. These authors succeeded in obtaining chemical laser oscillation by exploiting the $[\text{O}_2(^1\Delta_g)]_2 \rightarrow [\text{O}_2(^3\Sigma_g^-)_{v=0} + \text{O}_2(^3\Sigma_g^-)_{v=1}]$ transition centered at 703 nm. In another domain, this emission may serve to determine the $\text{O}_2(^1\Delta_g)$ concentration.¹⁹

The interest of the O_2 complex, in particular for atmospheric implications, has motivated a large number of experimental studies (see Refs. 6, 7, 19–22, and references therein). The atmospheric spectrum exhibits several weak absorption bands arising from collisional induced absorption by oxygen in the infrared, the red, the blue, and the near ultraviolet regions.²² Recent progress was achieved in the analysis of the collision-induced absorption of O_2 in the infrared^{23,24} and a novel complex $[\text{O}_2(X^3\Sigma_g^-) + \text{O}_2(c^1\Sigma_u^-)]$ was identified.^{25,26}

Absorption bands associated with colliding O_2 molecules appear broad and structureless due to the short duration of a collision. According to Ref. 27, the absorption due to the bound species should roughly follow the magnitude of the collision induced absorption. Therefore narrow but weak structures, revealing the existence of a bound species, are expected to be superimposed on all these diffuse bands, but should be more easily observable for the strongest ones in the visible (at 578 and 630 nm) and in the near infrared (at 1.06 and 1.26 μm). The first evidence of a bound electronic state of $(\text{O}_2)_2$ was provided by Long and Ewing²⁸ 25 years ago; they recorded low resolution gas phase spectra in the visible and in the infrared at a temperature of 87 K and with a pathlength of 200 m. They assigned narrow features, superimposed on the collision induced absorption band at 578 nm, to $(\text{O}_2)_2$. A vibrational assignment was proposed but the limited resolution of this experiment did not allow any rotational analysis.²⁸ Considering the weakness of the narrow features observed by Long and Ewing, high sensitivity absorption methods are required to detect and rotationally resolve the spectrum. In this context, we have recently applied IntraCavity Laser Absorption Spectroscopy (ICLAS) coupled with a supersonic jet to the detection of the O_2 dimer.⁶ Two rovibronic bands near 578 and 632 nm of $(\text{O}_2)_2$ were rotationally resolved for the first time. The spectrum at 578 nm was also obtained by ICLAS in a cell of oxygen cooled to liquid nitrogen temperature⁶ confirming the attribution to $(\text{O}_2)_2$ of the narrow features observed by Long and Ewing. The first band lying at 578 nm and noted hereafter (1–0) corresponds to the simultaneous excitation of two oxygen molecules from the ground state to the same electronic excited state with an additional vibrational excitation for one of the monomers $[\text{O}_2(^1\Delta_g)_{v=0} + \text{O}_2(^1\Delta_g)_{v=1}] \leftarrow [\text{O}_2(^3\Sigma_g^-)_{v=0}]_2$. The second band at 632.6 nm, noted (0–0), is weaker and corresponds to the $[\text{O}_2(^1\Delta_g)_{v=0}]_2 \leftarrow [\text{O}_2(^3\Sigma_g^-)_{v=0}]_2$ transition.

The equilibrium configuration of $(\text{O}_2)_2$ was discussed by Long and Ewing who formulated the hypothesis of a floppy structure for this dimer.²⁸ A few years later, Goodman and Brus determined that the H geometry is the most stable struc-

ture of the dimer when isolated in a neon matrix.²⁹ Long and Ewing estimated the well depth to be about 80 cm^{-1} ,²⁸ assuming a Lennard-Jones intermolecular potential as previously suggested by Stogryn and Hirschfelder.³⁰ This value is in good agreement with our recent estimation of the ground state dissociation energy from the extension of the highly congested rotational structure.⁶ It also agrees reasonably well with the potential energy surface calculated by Bussery *et al.*³¹ in the case of a planar rectangular H geometry of the dimer. Indeed, these calculations predicted that the H geometry is the most stable for the ground singlet and triplet states, whereas the strongest binding energy for the quintuplet state is associated with the X geometry. The H and crossed X geometries are predicted equally probable for the four singlet states dissociating into $[\text{O}_2(^1\Delta_g) + \text{O}_2(^1\Delta_g)]$. Well depths of 154, 140, and 126 cm^{-1} are calculated for the ground singlet, triplet, and quintuplet states, respectively. These different geometrical structures result from the weaker core repulsion when the two monomers get closer to each other in parallel configurations, and allows the attractive long range interactions to increase their potential well. Furthermore, the triplet–triplet spin interaction between the two $\text{O}_2(^3\Sigma_g^-)$ monomers is stronger and antiferromagnetic for the H geometry due to a maximum of orbital overlap while weaker and ferromagnetic for the X geometry. As a consequence, it results a ground singlet state for the dimer in the H geometry.³¹

The floppy character of the dimer is highlighted by the weak predicted torsional barrier of about 35 cm^{-1} for the singlet ground state and of a few cm^{-1} for the excited singlet states.^{32–34}

The limited signal to noise ratio achieved in our preliminary ICLAS experiments and the congestion of the spectrum made a rotational analysis of the early spectrum impossible.⁶ The spectral resolution was limited by the spectrograph dispersing the laser spectrum resulting also in a loss of sensitivity. This stimulated us to investigate the (0–0) band in a slit jet expansion by Continuous Wave Cavity Ring Down Spectroscopy (CW-CRDS) which allows sub-Doppler resolution. The CRDS technique has been employed as a diagnostic tool³⁵ to detect or measure concentration of radicals.^{36,37} For instance, some of us detected recently by pulsed CRDS, the first ionized gas-phase spectrum of a polycyclic aromatic hydrocarbon in a supersonic slit jet coupled with an ionizing discharge.³⁸ The sensitivity and resolution of the CRDS technique can be increased by the use of CW lasers for injection of light³⁹ which allows sub-Doppler resolution recordings⁴⁰ besides broadband continuum measurements⁴¹ as the pulsed implementation.

We report hereafter the high resolution study of the (0–0) band of $(\text{O}_2)_2$ recorded near 632.6 nm by CW-CRDS with an external cavity diode laser source. The same spectrum was also recorded by a newly built ICLAS spectrometer associated with a supersonic slit jet for comparison. After the description and discussion of the experimental techniques in Sec. II, we will present in Sec. III the first rotational analysis of several subbands of the (0–0) band based on full quantum dynamical calculations of the O_2 dimer.^{42,43} The rotational analysis, based on CW-CRDS data, will lead to the determi-

nation of the rotational temperature of the (O₂)₂ molecules. We will then discuss in Sec. IV the geometry of the dimer in its ground and excited electronic states and propose a vibrational assignment of the whole spectrum.

II. EXPERIMENT

A. CW-CRDS

The CRDS technique is based on the measurement of the decay rate of photons trapped in an optical cavity containing the absorber.⁴⁴ In CW-CRDS, the injection of photons occurs when the optical frequency of a narrowband cw-laser coincides exactly with one of the cavity modes. This is achieved repeatedly by using a piezoelectric transducer which modulates the cavity length.³⁹ CW-CRDS allows a very high resolution and sensitivity compared to a standard pulsed-CRDS implementation. The setup used for the present experiment was essentially the same as the one used in the first diode laser CW-CRDS experiment.³⁹ An external cavity diode laser (EOSI, 5 mW @ 632 nm) was used to inject photons in the high finesse passive cavity. The laser was mode-matched to the cavity leading to a significant improvement of the signal to noise ratio.³⁹ After mode matching, the ratio of transverse to longitudinal mode excitation was measured to be 1:200. A cavity photon lifetime τ of about 15 μ s was measured, corresponding to a reflectivity $R \sim 0.9999$. The two supermirrors (Research Electro Optics) were mounted on a $L = 50$ cm wide jet chamber equipped with a $l = 24$ cm long and 12 μ m wide slit to increase the absorption path-length. According to Nesbitt *et al.*,⁴⁵ the use of a slit, rather than a nozzle, results in an increase of the number of collisions and then favors the dimer formation. We applied a continuous stagnation pressure of pure O₂ (Air Liquide, 99.5% purity) ranging from 1 to 5 bar at room temperature, corresponding to a background pressure in the cavity between 0.7 and 3.6 mbar. The maximum dimer absorption signal was obtained at a distance of 2.5 mm from the slit aperture which was estimated to be still far from the Mach disk. Figure 1 shows an overview of the spectrum recorded between 15 800 and 15 860 cm^{-1} at a jet stagnation pressure of 2.7 bar.

The ratio of the intensity of the dimer lines to the baseline noise increased up to a stagnation pressure of about 2.7 bar. The increase of the noise level at higher pressures, evident in Fig. 2, may be due to jet turbulences. The acquisition rate was maintained at 200 Hz for that stagnation pressure. An avalanche photodetector was employed to monitor the signal. A noise level of about 4×10^{-9} /cm (or 2×10^{-9} /cm for the full cavity length), as shown on Fig. 1, was achieved by averaging 20 ringdown events for each data point. The scanning step was chosen sufficiently small (every 20 MHz) in order to accurately probe the sub-Doppler line profiles (250 MHz FWHM). A 13 points Savitsky–Golay smoothing⁴⁶ was also applied to the data without lineshape distortion, further reducing the noise by a factor of 2.5.

For each laser scan ($\sim 3.6 \text{ cm}^{-1}$ acquired in 10 min), we recorded simultaneously étalon fringes and an iodine absorption spectrum using silicon photodiodes. The sinusoidal étalon fringes (0.115 cm^{-1} free spectral range) were used for

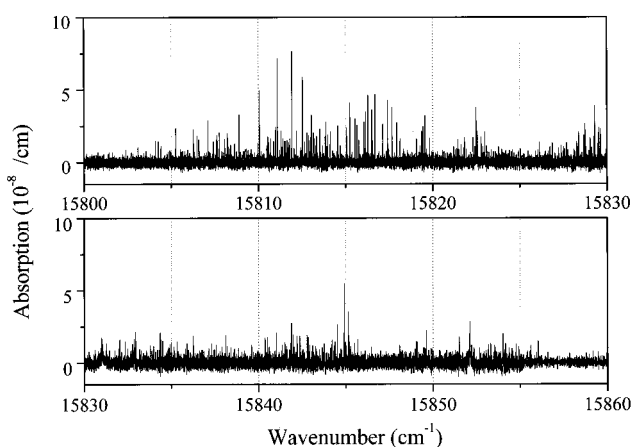


FIG. 1. Overview of the CW-CRDS jet spectrum of the O₂ dimer. Recordings were performed at a stagnation pressure of 2.7 bar and at distance of 2.5 mm from the slit. More than 600 lines which exhibit a typical width of 200 MHz, were measured above a noise threshold of 4×10^{-9} /cm taking into account of the filling ratio of the cavity (the absorption coefficient is given by $1/(l/L)c\tau$, with τ , the ringdown time).

linearisation of the frequency scale and the detection of possible laser mode hops. Two iodine lines in each scan were used as reference for the absolute calibration.^{47,48} Finally, we had to take into account the frequency shift f induced by the acousto optic modulator as the laser beam probed the molecule at a frequency of $\nu + f$, whereas the reference signal had no frequency shift. In this condition, a frequency shift of $f = 80$ MHz was subtracted. From a series of recordings, we estimated the absolute accuracy of the calibration to be better than $\pm 0.002 \text{ cm}^{-1}$ (60 MHz).

The O₂ rotational temperature was estimated to be 20 ± 15 K for a stagnation pressure of 2.7 bar from the intensity of three lines lying in the vicinity of the dimer spectrum, namely, $^P P(1)$, $^P Q(2)$, and $^P P(3)$ lines of the $b^1 \Sigma_g^+(v=2) \leftarrow \tilde{X}^3 \Sigma_g^-(v=0)$ rovibronic transition.⁴⁹ The gaseous oxygen O₂ total absorbance, αL , results from the contribution of jet cooled oxygen $\alpha^{\text{jet}l}$ (in the active zone) and ab-

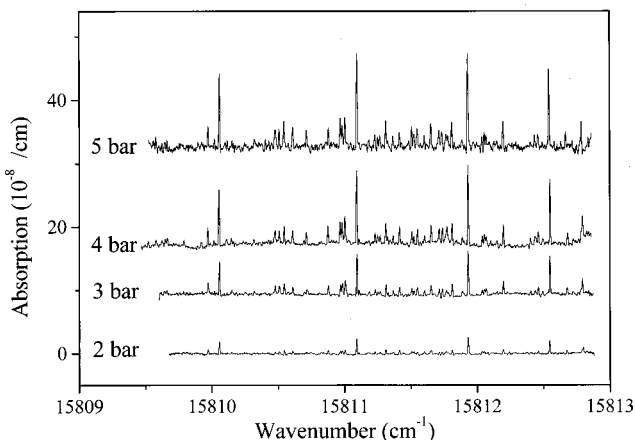


FIG. 2. Study of the dependence of the oxygen dimer absorption spectra vs the jet stagnation pressure of pure oxygen. The relative intensity distribution does not change with the pressure indicating a weak dependence of the rotational temperature. The zero baseline is shifted for convenience. A weak distortion of the baseline is observed for pressure above 3 bar.

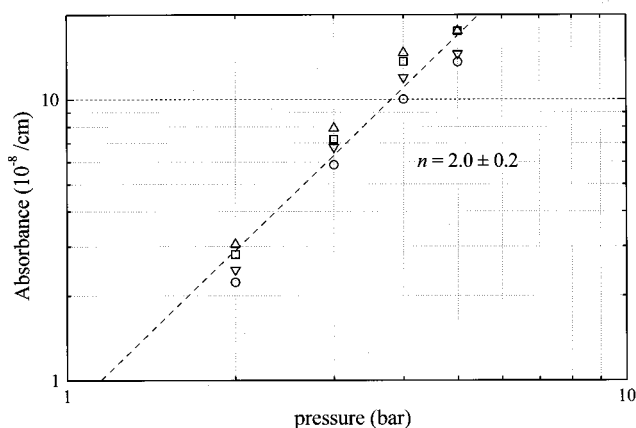


FIG. 3. Dependence of the O_2 dimer absorption vs the stagnation pressure (logarithm scale). Each series represents the evolution of the intensity of four strong Q lines.

sorption due to background room temperature oxygen $\alpha^{bk}(L-l)$. We were able to estimate the intensity of the absorption lines due to O_2 in the jet by separately fitting the room temperature profiles from the superposed jet temperature profiles. The value of 20 K obtained for the rotational temperature will be confirmed and refined hereafter using line intensities of the O_2 dimer itself after their rotational assignment.

As a consequence of the bimolecular reaction leading to the formation of the dimer,⁵⁰ the concentration of $(O_2)_2$, and consequently the intensity of its absorption spectrum, is expected to be a quadratic function of the pressure at least for low stagnation pressures. Figure 2 shows that the relative line intensities are not sensitive to the stagnation pressure indicating a weak dependence of the rotational temperature versus the pressure in the 2–5 bar range. From Fig. 3 which shows, in a logarithm scale, the evolution of the intensities of four strong lines vs the pressure, we derived a slope $n=2.0 \pm 0.2$. Nevertheless, recent kinetics calculations from Vigasin,⁵¹ which also include the trimerization of the O_2 molecules, show that the concentration of the dimers follow a quadratic dependence only up to a pressure of 4 bars. For higher pressures, the increase is slower as a consequence of the formation of clusters larger than dimers.

B. ICLAS

An improved ICLAS spectrometer, based on a ring dye laser, allowing increased performances in terms of resolution and sensitivity compared to our previous investigation (see, in particular, Fig. 4 in Ref. 6), has been developed in order to record the same spectrum with an expected signal to noise ratio comparable to CW-CRDS. Indeed, ICLAS is a very sensitive technique which has demonstrated the ability to achieve absorption coefficient of $10^{-10}/\text{cm}$ with a ring laser configuration.⁵² This technique has proven its efficiency in particular when coupled with a supersonic jet.⁵³ The limitation, in our previous investigation of the O_2 dimer,⁶ arose partly from the large spacing between laser modes compared to the narrow absorption linewidth. If the mode frequencies fluctuate sufficiently during the acquisition, narrow absorp-

tion lines (typically 250 MHz in a slit-jet expansion) are averaged. As part of time the absorption lines fall in between laser modes (150 MHz free spectral range in our preceding linear configuration), there is a loss of signal and thus of sensitivity.⁵³ Besides its improved sensitivity, the second advantage of our ring configuration lies in the enlargement of the cavity which decreases the free spectral range and then favors a more continuous sampling of the absorption lines. The only serious drawback of the present configuration was the lower filling ratio of the cavity compared to CW-CRDS (about 10 times) which was partly compensated by operating at a stagnation pressure of $2.7 \times \sqrt{10} \approx 9$ bar as the absorption signal depends roughly on the pressure squared.

The pressure could be increased by pulsing the jet since higher pressures can be used in a pulsed regime than in a continuous mode as a consequence of the stagnation pressure upper limit fixed at 5 bar by the pump system capacity. Note that a pulsed scheme could also be applied with CW-CRDS, nevertheless resulting in an important increase of the acquisition time. The timing scheme of the ICLAS data acquisition has been previously described.⁵³ The jet was pulsed during periods of about 10 s, followed by a delay three times longer. The spectral multiplex ability of ICLAS avoids a large consumption of gas as the spectrum (about 18 cm^{-1}) was obtained in a few jet pulses (~ 60 s) whereas the recording of the same spectral window required about 50 min with CW-CRDS. A high resolution CCD (3724 pixels) has been employed to record the laser spectrum at the focal plane of the grating spectrograph. This increased the resolution of the recordings while keeping the same spectral window as previously.⁶ The O_2 dimer spectral linewidth, limited by the apparatus function, was measured to be about 650 MHz (FWHM), i.e., 2.5 times the residual Doppler linewidth measured by CW-CRDS.

As with the CRDS experiments, we used sharp fringes of a Fabry–Perot étalon, inserted when needed in the cavity, for frequency linearization. Two iodine lines^{47,48} were used as reference for absolute frequency calibration.

A series of ICLAS measurements showed the spectra to be reproducible with minor oscillation of the baseline. The relative intensities of all the strong lines were comparable to the CW-CRDS spectrum. Figure 4 shows a comparison of CW-CRDS and ICLAS spectra recorded at a stagnation pressure of 2.7 and 9 bar, respectively. A noise level of $2 \times 10^{-8}/\text{cm}$ (or $10^{-9}/\text{cm}$ for the full cavity length) was measured from the ICLAS spectrum (Fig. 4) recorded with a typical generation time t_g of 1 ms. This limited performance, at least one order of magnitude worse than expected, may result from the fluctuations of the supersonic jet expansion due to the formation of large clusters.

In consequence, the forthcoming rotational analysis will be based on the CW-CRDS spectra only. However, this work constitutes a good illustration of the complementarity of ICLAS and CW-CRDS techniques. In fact, we see that in general ICLAS may be very useful in exploring large spectral regions, limiting gas consumption when using a slit jet supersonic expansion. On the other hand, CW-CRDS is suitable when more detailed investigation is needed, since it al-

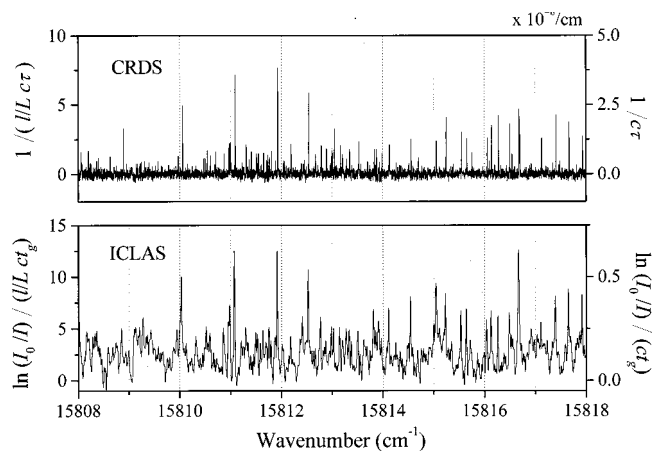


FIG. 4. Part of the CW-CRDS and ICLAS spectrum of (O₂)₂ recorded at jet stagnation pressures of 2.7 and 9 bar, respectively. The right scales correspond to the measured decay rate of the cavity (CW-CRDS) and to the frequency selective losses due to the whole cavity (ICLAS), whereas the left scales correspond to the (O₂)₂ absorption when we take into account the filling ratio l/L of the cavity of 50% (CW-CRDS) and 5% (ICLAS). Note also that the ICLAS spectrometer induces an apparent broadening of about three times the residual sub-Doppler width measured by CW-CRDS.

lows a higher resolution and consequently higher sensitivity at sub-Doppler resolution.

III. RESULTS

About 600 lines are measured from the CW-CRDS spectrum recorded between 15 800 and 15 860 cm⁻¹ with a stagnation pressure of 2.7 bar (see Fig. 1). A schematic representation of the O₂ dimer structure indicating the three axes of inertia (with $I_A < I_B < I_C$) is given in Fig. 5, when the dimer is in the planar rectangular H ($\theta_A = \theta_B = 90^\circ, \varphi = 0^\circ$) geometry. This is the structure predicted by theoretical calculations^{31,54,55} to be the most stable for the singlet and triplet ground states of the dimer, while the H and the crossed X ($\theta_A = \theta_B = \varphi = 90^\circ$) geometries are equivalently probable for the excited states.^{33,34} Based on semiempirical potential energy surfaces, full quantum calculations of the rovibrational structure of both states involved in the present transition have been conducted accounting only for the ground singlet state of $[\text{O}_2(^3\Sigma_g^-)]_2$ and for the singlet excited states of $[\text{O}_2(^1\Delta_g)]_2$ as the singlet \leftarrow triplet and singlet \leftarrow quintet transitions are forbidden in a first approximation.^{31,33} These calculations have shown that for a given K value, the J sequences follow the same progression than those of a prolate slightly asymmetric top semirigid molecule with the rotational energy levels given by (for low values of J)

$$F(J, K) = \frac{B+C}{2} J(J+1) + \left(A - \frac{B+C}{2} \right) K^2, \quad (1)$$

where K is the projection of the total angular momentum J on the axis joining the centers of mass of the two monomers. We note that K is a good quantum number in the symmetric top limiting case ($K = K_A$) and when neglecting Coriolis interactions. As the calculated rovibrational levels verify satis-

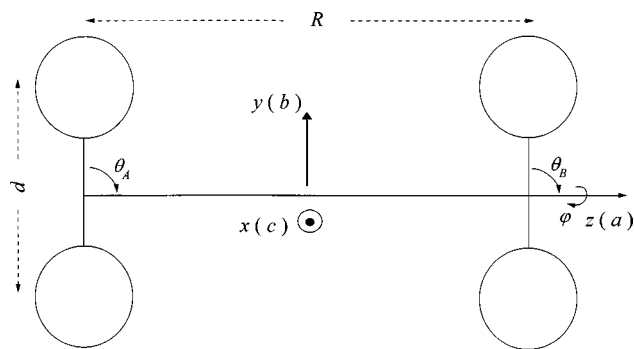


FIG. 5. Schematic representation of the (O₂)₂ in its rectangular H geometry ($\theta_A = \theta_B = 90^\circ, \varphi = 0^\circ$). The three axes of the inertia moment are given. R is the distance between the center-of-mass of the monomers and d is the interatomic distance for the monomers.

factorily the progression in J but not in K , different effective rotational constants may be obtained for each K value. Then we note,

$$F_K(J) = \frac{B+C}{2} J(J+1). \quad (2)$$

A. Assignment procedure

The initial identification is based on the presence of series of strong Q lines which should dominate the spectrum. Indeed, for a slightly asymmetric top semi-rigid molecule, the Q branch is expected to be approximately twice as intense as the R or P branch.⁵⁶ As no rotational analysis was previously reported, the selection of lines at the onset is performed on the basis of theoretical results.^{42,43} Due to the floppy character of the O₂ dimer, as first suggested by Long and Ewing²⁸ and confirmed by theoretical calculations,^{31,33} the symmetry of the rovibrational levels is labeled in the G_{16} permutation inversion group⁵⁷ instead of an usual point group employed with rigid molecules. Furthermore, with a zero nuclear spin for the oxygen atom, permutations between

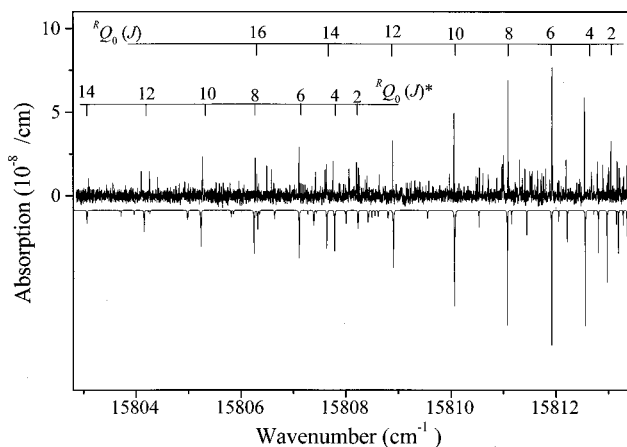


FIG. 6. Part of the CW-CRDS spectrum of (O₂)₂ which shows two subbands corresponding to $[(v'_1=0, v'_2=1), K'=1]B_1^- \leftarrow [(v_1=0, v_2=0), K=0]A_1^+$ and $[(0,0), 1]A_1^+ \leftarrow [(0,1), 0]B_1^-$ transitions, the asterisk referring to the latter. Only the Q branches assignment is given. The simulation on the lower part was calculated at 12 K with the experimental relative intensity for the P , Q , and R branches.

TABLE I. Wave numbers, rotational assignment, and residuals of the transitions of the $K'=1 \leftarrow K=0$ subband ($B_1^- \leftarrow A_1^+$) of $(\text{O}_2)_2$ centered at $15\,813.13\text{ cm}^{-1}$. The line wave numbers were included in the fit with a weight proportional to the square of their relative intensity (see text). The lines marked with an asterisk (*) are perturbed and excluded from the fit.

J	${}^R P_0(J)$	obs-calc	${}^R Q_0(J)$	obs-calc	${}^R R_0(J)$	obs-calc
0					15 813.284	0.023
2	15 812.772	0.070	15 813.041*	0.085	15 813.337	-0.001
4	15 812.026	-0.011	15 812.534	-0.010	15 813.158	-0.020
6	15 811.218	0.068	15 811.919	0.008	15 812.784	-0.014
8	15 810.141	0.081	15 811.079	0.005	15 812.184	-0.031
10	15 808.740	-0.050	15 810.046	-0.012	15 811.496	0.044
12	15 807.340	-0.032	15 808.880	-0.013	15 810.597*	0.056
14			15 807.620	-0.002	15 809.512	-0.011
16			15 806.292	-0.016		

the atoms inside the monomers and between the two monomers must be even, so that only A_1^+ and B_1^- symmetries are physically allowed for the $[\text{O}_2(^3\Sigma_g^-)_{(v=0)}]_2$ and $[\text{O}_2(^1\Delta_g)_{(v=0)}]_2$ dimers.^{32,42} In this G_{16} representation, the electric dipole selection rules impose $B_1^- \leftarrow A_1^+$ and $A_1^+ \leftarrow B_1^-$ with $\Delta J=0, \pm 1$ and $\Delta K = \pm 1$.³² In the ground electronic state, the lowest rovibrational level of A_1^+ symmetry ($K=0, J=0$) is calculated about 6.9 cm^{-1} below the lowest level of B_1^- symmetry ($K=0, J=0$).⁴² Then given the low temperature of the supersonic slit jet expansion, the expected most intense transitions correspond to $\Delta K = +1$ subbands with $K=0$ for the lower state as the lowest and most populated state is the $K=0$ level of A_1^+ symmetry. The assignment is initiated by considering that the stronger lines are the ${}^R Q_0(J)$ lines with even J values since rotational levels for $K=0$ with odd J values are calculated at higher energy for symmetry reasons^{32,42} and are then not observable. The wave number of a given transition, introducing the centrifugal distortion constants D and D' , can be written as⁵⁶

$$\nu = \nu_0 + \frac{B' + C'}{2} J'(J' + 1) - \frac{B + C}{2} J(J + 1) + DJ^2(J + 1)^2 - D' J'^2(J' + 1)^2, \quad (3)$$

where

$$\nu_0 = F_{K'}(J' = 0) - F_K(J = 0). \quad (4)$$

TABLE II. Wave numbers, rotational assignment, and residuals of the transitions of the $K'=1 \leftarrow K=0$ subband ($A_1^+ \leftarrow B_1^-$) of $(\text{O}_2)_2$ centered at $15\,808.40\text{ cm}^{-1}$. The line wave numbers were included in the fit with a weight proportional to the square of their relative intensity (see text). The ${}^R Q_0(12)$ line marked with an asterisk (*) is perturbed and excluded from the fitting procedure.

J	${}^R P_0(J)$	obs-calc	${}^R Q_0(J)$	obs-calc	${}^R R_0(J)$	obs-calc
2	15 807.979	0.027	15 808.244	0.036	15 808.622	0.030
4	15 807.220	-0.037	15 807.743	-0.026	15 808.387	-0.022
6	15 806.323	-0.013	15 807.096	-0.008	15 808.046	0.046
8	15 805.290	0.065	15 806.257	0.008	15 807.411	0.001
10	15 804.021	0.051	15 805.252	0.002	15 806.611	-0.047
12			15 804.087*	-0.081	15 805.775	-0.057
14			15 803.078	0.003		

The assignment of the regular series of lines dominating the spectrum (see Fig. 6) to the ${}^R Q_0$ branch of $B_1^- \leftarrow A_1^+$ type is relatively straightforward. The associated ${}^R R_0$ and ${}^R P_0$ branches are extracted with more difficulty because of superpositions and weaker intensity. Finally 22 transitions, given in Table I, can be assigned to this subband centered at $15\,813.13\text{ cm}^{-1}$. In a second step, 18 transitions of a subband centered at $15\,808.40\text{ cm}^{-1}$, given in Table II, are identified and have been assigned to a $A_1^+ \leftarrow B_1^-$ type transition from the lowest $K=0$ level of B_1^- symmetry. The observed line positions of the two $K=0$ subbands given in Tables I and II were used to determine the values of the ν_0 , $B_p = (B + C)/2$ and D constants [see Eq. (3)]. The fitting procedure shows that for both subbands, the ${}^R Q_0(J)$ line positions are more satisfactorily reproduced by Eq. (3) than the ${}^R P_0(J)$ and ${}^R R_0(J)$ line positions. This result clearly indicates the limit of validity of the expression of the rotational energy levels used in the present analysis. In consequence, in the global fit of the P , Q , and R line positions, we choose to give a higher weight to the ${}^R Q_0(J)$ lines, which are the strongest ones, by affecting to the wave numbers a weight proportional to the square of the relative line intensity. Following this procedure, we obtain the values of the rovibrational parameters listed in Table III. As a consequence of the strong correlation between the distortion constants, the value of D' , which is expected to be smaller than D , is constrained to zero leading to an effective distortion term $D_{\text{eff}} J^2(J + 1)^2$, where D_{eff} is very close to $D - D'$. For both subbands, the weighted root mean square deviation achieved is of the order of 0.02 cm^{-1} , i.e., about one order of magnitude larger than our wave number accuracy. This result obtained after excluding some clearly perturbed lines (see Tables I and II and Fig. 7) shows that the model used for the rotational analysis is probably over simplified. Furthermore, the quality of the fit is probably affected by the occurrence of perturbations due to the large density of possibly interacting rovibrational levels, in particular in the excited state. A global fit performed by affecting the same weight to all the assigned lines leads to a rms error of 0.035 cm^{-1} (instead of 0.014 cm^{-1}) but leaves practically unchanged the values of the rovibrational parameters ν_0 , B_p , and D . The most significant change between the two fits is a slight shift of 0.02 cm^{-1} for the band center of the first band [$15\,813.153(70)$ instead of $15\,813.134(37)\text{ cm}^{-1}$ for the weighted fit].

Table III shows the satisfactory agreement of the experimentally determined rotational constant values with the predicted ones obtained by integrating over the whole potential energy surface.^{42,43} The consistency of our analysis is also sustained by the very close value of the rotational constants obtained for the two subbands under consideration.

As only the lowest levels of the ground state are assumed to be populated, the subbands lying in the $15\,810\text{--}15\,820\text{ cm}^{-1}$ region should have an upper level corresponding to the lowest energy levels of the $[\text{O}_2(^1\Delta_g)_{v=0}]_2$ electronic state and are then expected to be less perturbed than those closer to the dissociation limit (i.e., in the blue part of the spectrum). We succeeded however in assigning Q lines of another subband centered at $15\,818.28\text{ cm}^{-1}$ shown in Fig. 8. The fit of the line positions of this subband, listed

TABLE III. Rovibrational parameters of the lowest vibrational levels of [O₂(³Σ_g⁻)_(v=0)]₂ and [O₂(¹Δ_g)_(v=0)]₂.

		ν_0	B'_p	B_p	ΔB_p	$D_{\text{eff}} \times 10^{-4}$	rms
$K' = 1 \leftarrow K = 0$							
$B_1^- \leftarrow A_1^+$	obs	15 813.134(37)	0.0634(27)	0.0932(28)	-0.0298	0.170(40)	0.0140
	calc ^a		0.0604	0.0856	-0.0252		
$A_1^+ \leftarrow B_1^-$	obs	15 808.401(49)	0.0640(30)	0.0962(34)	-0.0322	0.328(70)	0.0210
	calc ^a		0.0601	0.0837	-0.0236		
$K' = 1 \leftarrow K = 2$							
$B_1^- \leftarrow A_1^+$	obs	fit1 ^b 15 818.277(35)			-0.0297(19)	0.19(4)	0.015
		fit2 ^c 15 818.276(38)	0.0621(16)	0.0918(21)	-0.0297	0.19(6)	0.018
$A_1^+ \leftarrow B_1^-$	calc ^a			0.0853			
	obs	fit1 ^b 15 812.656(20)			-0.0298(23)	0 ^d	0.011
		fit2 ^c 15 812.666(34)	0.0635(24)	0.0934(24)	-0.0299	0 ^d	0.018
	calc ^a			0.0847			

^aCalculated value from Refs. 42 and 43.^bOnly the Q branch was fitted.^cThe P , Q , and R line positions were included in the fit with equivalent weight.^dConstrained to zero.

in Table IV, shows that the higher energy line at 15 818.119 cm⁻¹ should be assigned to $Q(2)$. As showed in Fig. 8, the absence of the $Q(1)$ line indicates that this subband probably arises from $K=2$ levels since all $Q(J)$ lines with even and odd J values (except $J=0$ and 1) are observed.

Quantum calculations which predict a strong energetic shift of the $K=1$ levels in the electronic ground state confirm the hypothesis of excluding the $K=1$ levels (see Fig. 2 of Ref. 42). Indeed, the lower K levels are calculated at 0.0 cm⁻¹ ($K=0$), 26.2 cm⁻¹ ($K=1$), 2.3 cm⁻¹ ($K=2$) for the A_1^+ symmetry levels and 6.9 cm⁻¹ ($K=0$), 29.1 cm⁻¹ ($K=1$), 16.1 cm⁻¹ ($K=2$) for the B_1^- symmetry levels. We then believe that the lower state is the lowest $K=2$ level of A_1^+ symmetry whereas the upper level corresponds to $K'=1$ and not $K'=3$ as a consequence of the existence of a $Q(J=2)$ line (Table V). Finally, we tentatively assigned a fourth Q branch centered at 15 812.67 cm⁻¹ to the ${}^P Q_2$ branch of a $A_1^+ \leftarrow B_1^-$ band. Similarly to the two $K=0$ subbands, both $K=2$ subbands show that the Q branch is much

stronger than the R and P branches (see Table VI). In the case of the $K=2$ subband at 15 812.67 cm⁻¹, the P branch is even too weak to be detected.

The fitting procedure of the rovibrational parameters lead to a rms error of the order of 0.015 cm⁻¹. We give in Table III the values of the parameters obtained from the fit of the line positions of the ${}^P Q_2(J)$ lines only (fit1) and from the global (and nonweighted) fit including all data (fit2). The inclusion of the very weak ${}^P P_2(J)$ and ${}^P R_2(J)$ lines (some of them are tentatively assigned) in the fit (fit2 in Tables IV and V) leads to very similar, though less accurate, values of ν_0 , ΔB_p , and D_{eff} and allows B'_p and B_p to be determined independently. Table III shows that the values obtained for the B rotational constants of the four analyzed subbands are very close as theoretically predicted.^{32,42,43}

B. Determination of the rotational temperature

After rotational assignment, the line intensity distribution within the two $K=0$ subbands may be used for an ac-

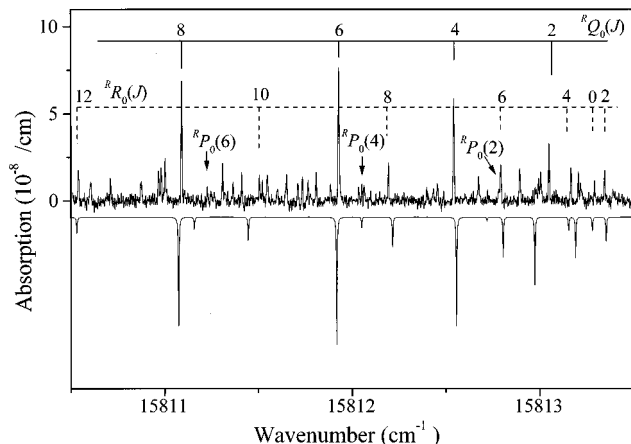


FIG. 7. Details of the CW-CRDS spectrum in the range of the Q branch of the subband centered at 15 813.134(37) cm⁻¹ which corresponds to $[(v'_1=0, v'_2=0), K'=1]A_1^+ \leftarrow [(0,1), 0]B_1^-$ transition. Note that the $Q(2)$ line is strongly perturbed.

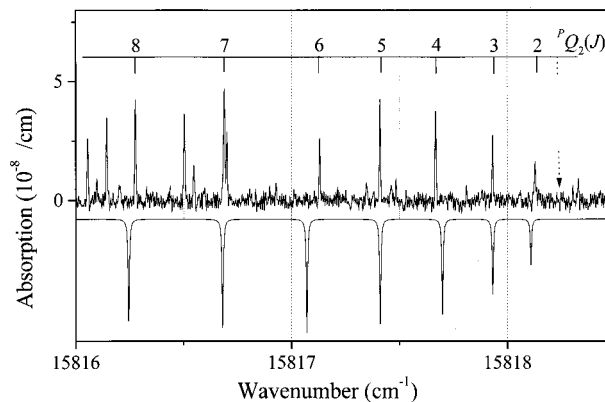


FIG. 8. Part of the CW-CRDS spectrum showing the Q branch of the subband centered at 15 818.28 cm⁻¹ corresponding to the $[(v'_1, v'_2), K'=1]B_1^- \leftarrow [(0,0), 2]A_1^+$ transition. The assignment of the Q branch is given. The absence of the $Q(1)$ line, as shown on the lower part of the plot, rules out a $K'=0 \leftarrow K=1$ transition. The lower part of the plot shows a simulation of the spectrum at a temperature of 12 K based on fit2. Note that the $Q(6)$ line is strongly perturbed.

TABLE IV. Wave numbers, rotational assignment, and residuals of the transitions of the $K'=1 \leftarrow K=2$ subband ($B_1^- \leftarrow A_1^+$) of $(O_2)_2$ centered at $15\,818.28\text{ cm}^{-1}$. Fit1 corresponds to the fit of the ${}^P Q_2(J)$ lines only, while fit2 is a global fit where the ${}^P P_2(J)$, ${}^P Q_2(J)$, and ${}^P R_2(J)$ lines were included with an equivalent weight. Lines marked with an asterisk (*) are blended or perturbed, excluded from the fitting procedure.

J	${}^P P_2(J)$		${}^P Q_2(J)$			${}^P R_2(J)$	
	obs	obs-calc	obs	obs-calc		obs	obs-calc
		fit2		fit1	fit2		fit2
2	15 817.874	0.0223	15 818.119	0.019	0.020	15 818.475	0.003
3	15 817.522	-0.028	15 817.923	0.001	0.000	15 818.423	0.003
4	15 817.205	0.017	15 817.658	-0.033	-0.032	15 818.316	0.005
5	15 816.796	0.014	15 817.401	0.003	-0.002	15 818.119	-0.029
6	15 816.319	0.001	15 817.121*	0.056	0.057	15 817.923	-0.01
7			15 816.692	0.015	0.017	15 817.658	-0.01
8			15 816.266	0.026	0.028	15 817.375	-0.008
9			15 815.745	-0.017	-0.015	15 817.002	-0.001
10			15 815.236	-0.008	-0.007	15 816.582	-0.028
11			15 814.693	0.000	0.001	15 816.220	0.036
12			15 814.109	-0.003	-0.004		
13			15 813.512	0.004	0.002		
14			15 812.885	-0.002	-0.006		

curate determination of the rotational temperature of $(O_2)_2$ in the jet. For a prolate symmetric top molecule with perpendicular absorption bands, the intensity distribution of the rotational structure is given by⁵⁶

$$I_{KJ} = C \nu A_{KJ} g_{KJ} \exp\left(-\frac{F_K(J)}{kT}\right), \quad (5)$$

where A_{KJ} is the Hönl–London factor in the case of a semi-rigid rotor, g_{KJ} is the statistical weight of the ground state, ν is the wave number, and C is a constant proportional to the square of the transition moment of the band. As the observed transitions are spread over a limited wave number range, $C\nu$ can be considered as a constant. Let us examine the two $K=0$ subbands which are sufficiently intense to allow good relative intensity measurements. For $K=0$, the product $A_{KJ} g_{KJ}$ equals $J-1$, $2J+1$, and $J+2$ for the P , Q , and R branches, respectively.⁵⁶ By plotting for each branch the

TABLE V. Wave numbers, rotational assignment, and residuals of the transitions of the $K'=1 \leftarrow K=2$ subband ($A_1^+ \leftarrow B_1^-$) of $(O_2)_2$ centered at $15\,812.656(20)\text{ cm}^{-1}$. Fit1 corresponds to the fit of the ${}^P Q_2(J)$ lines only, while fit2 is a global fit where the ${}^P Q_2(J)$ and ${}^P R_2(J)$ lines were included with an equivalent weight. Lines marked with an asterisk (*) are blended or perturbed, excluded from the fitting procedure. The ${}^P P_2(J)$ lines were too weak to be detected.

J	${}^P Q_2(J)$			${}^P R_2(J)$	
	obs	obs-calc		obs	obs-calc
		fit1	fit2		fit2
2	15 812.480	0.003	-0.007	15 812.883*	0.034
3	15 812.389*	0.091	0.083	15 812.810	-0.005
4	15 812.054	-0.005	-0.014	15 812.716	0.013
5	15 811.756	-0.005	-0.012	15 812.534	0.004
6	15 811.400	-0.003	-0.009	15 812.267	-0.031
7	15 810.982	-0.004	-0.008	15 812.042	0.036
8	15 810.532	0.023	0.021	15 811.635	-0.02
9	15 809.961	-0.011	-0.012	15 811.237	-0.006
10	15 809.393	0.017	0.019		
11	15 808.709	-0.011	-0.007		

quantity $\ln(I_B/A_{KJ} g_{KJ})$ vs the lower state energy $F_{K=0}(J)$ obtained from Eq. (2), the rotational temperature T can be determined. Figure 9 shows the corresponding plots for the ${}^R P_0$, ${}^R Q_0$, and ${}^R R_0$ branches of the $B_1^- \leftarrow A_1^+$ subband leading to an average value of $12.1 \pm 0.9\text{ K}$. The similar determination of T from the ${}^R Q_0$ and ${}^R R_0$ branches of the $A_1^+ \leftarrow B_1^-$ subband, the ${}^R P_0$ branch being too weak to be considered, gives a value of $12.2 \pm 0.8\text{ K}$. The linear dependence observed in Fig. 9 and the good agreement between the five determinations of T strongly supports our rotational assignment. Note also that these values agree satisfactorily with our approximate determination of the rotational temperature from the O_2 transitions. Table VI shows that the integrated intensity of the P , Q , and R branches is measured to be in the ratio of 0.15:1:0.37 and 0.31:1:0.53 for the bands centered at $15\,813.13$ and $15\,808.40\text{ cm}^{-1}$, respectively while a ratio of 0.45:1:0.55 is calculated at 12 K from Eq. (5) in the semirigid rotor approximation. The observed weakness of the P branches may arise from a floppy molecule behavior of the O_2 dimer.⁵⁸

Figure 6 shows a comparison of a part of the CW-CRDS spectrum with a simulation of the two $K=0$ subbands. Each subband is simulated with a rotational temperature of 12 K determined above. The relative integrated intensities of the P , Q , and R branches are fixed to their experimental values, given in Table VI. The enlargement of the CW-CRDS spec-

TABLE VI. Average intensities of the branches for the four analyzed subbands ($\times 10^{-8}/\text{cm}$) calculated from all the observed unperturbed and non-blended lines in a branch.

	P	Q	R
$K'=1 \leftarrow K=0$			
$B_1^- \leftarrow A_1^+$	0.64	4.36	1.60
$A_1^+ \leftarrow B_1^-$	0.58	1.9	1.00
$K'=1 \leftarrow K=2$			
$B_1^- \leftarrow A_1^+$	0.50	2.34	0.48
$A_1^+ \leftarrow B_1^-$	<0.40	1.10	0.50

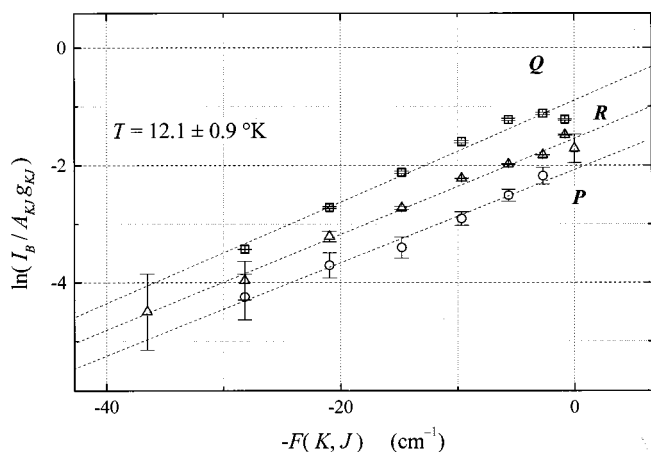


FIG. 9. Determination of the rotational temperature from the intensity distribution among the lines in the P_0 , Q_0 , and R_0 branches of the $B_1^- \leftarrow A_1^+$ subband centered at $15\,813.13\text{ cm}^{-1}$. The given error bars correspond to the uncertainty of the fitting line profiles.

trum, given in Fig. 7, in the range of the $^R Q_0$ branch of the $A_1^+ \leftarrow B_1^-$ subband shows the overall good agreement between the observed and simulated lines, despite a few perturbed line positions and a few relatively strong lines which remain unassigned. Figure 8 shows a similar simulation of the Q branch of the $K=2$ subband centered at $15\,818.28\text{ cm}^{-1}$ obtained from the results of fit2. The two $K=2$ subbands present various irregularities in the intensity of their rotational lines. The intensity distribution in the Q branch gives a rotational temperature T of $9.4 \pm 1.3\text{ K}$ and $9.7 \pm 1.6\text{ K}$ for the bands centered at $15\,818.28$ and $15\,812.66\text{ cm}^{-1}$, respectively, in reasonable agreement with previous determination.

IV. DISCUSSION

A. Structure of the O₂ dimer

Information on the dimer structure can be obtained from the comparison of the intermonomer distances, derived from

the rotational constant, with the theoretical values of the equilibrium distances.^{32,42,43} The rotational constant B_p is related to the O₂ bond length d , the mass of an oxygen atom m , and the intermonomer distance R_0 by (see Fig. 5),

$$B_p = \frac{\hbar}{4\pi c} \times \frac{1}{2} \left(\frac{1}{I_B} + \frac{1}{I_C} \right) \\ = \frac{\hbar}{8\pi c m} \left(\frac{1}{R_0^2} + \frac{1}{R_0^2 + d^2} \right) \\ \text{for the H}(\theta_A = \theta_B = 90^\circ, \varphi = 0^\circ) \text{ geometry,} \quad (6)$$

$$B_p = \frac{\hbar}{4\pi c m} \left(\frac{1}{R_0^2 + d^2/2} \right) \\ \text{for the X}(\theta_A = \theta_B = \varphi = 90^\circ) \text{ geometry,} \quad (7)$$

$$B_p = \frac{\hbar}{8\pi c m} \left(\frac{1}{R_0^2 + d^2} + \frac{1}{R_0^2 + d^2/2} \right) \\ \text{for the T}(\theta_A = 90^\circ, \theta_B = 0^\circ) \text{ geometry,} \quad (8)$$

and by,

$$B_p = \frac{\hbar}{4\pi c m} \left(\frac{1}{R_0^2 + d^2} \right) \\ \text{for the linear L}(\theta_A = \theta_B = 0^\circ) \text{ geometry.} \quad (9)$$

The O₂ bond length d , assumed to be unchanged compared to the free molecule, is $2.2884 a_0$ and $2.3043 a_0$ for the $^3\Sigma_g^-$ and $^1\Delta_g$ states, respectively.⁵⁹ Table VII gives the intermonomer distance R_0 in the ground and excited singlet states calculated for each possible geometry from the observed and predicted^{42,43} rotational constants. The theoretical values agree within 10% or better with the experimental values. As the intermonomer distance R_0 is expected to be approximately equal to or slightly larger than the equilibrium distance R_e , the comparison of the values given in Table VII rules out a linear or a T-shaped structure for the dimer in its ground singlet states. On the other hand, the R_0^{obs} value sup-

TABLE VII. Comparison of the intermonomer distance R_0 obtained from observed and calculated rotational constants of the lowest rovibrational levels (see the text). The equilibrium distance is also given. All values are in a_0 units.

Electronic state	Intermolecular distance	Level symmetry ^a		Geometry			
				H	X	T	L
[O ₂ ($^3\Sigma_g^-$) _{v=0}] ₂	R_0	A_1^+	obs	6.14	6.13	6.02	5.91
			calc ^b	6.44	6.43	6.33	6.22
	R_0	B_1^-	obs	6.04	6.02	5.92	5.80
			calc ^b	6.51	6.50	6.40	6.30
		R_e		calc ^c	6.10	6.30	7.60
[O ₂ ($^1\Delta_g$) _{v=0}] ₂	R_0	A_1^+	obs	7.53	7.53	7.44	7.35
			calc ^b	7.73	7.72	7.63	7.53
	R_0	B_1^-	obs	7.51	7.50	7.41	7.32
			calc ^b	7.75	7.74	7.65	7.56
		R_e		calc ^c	6.3–6.4	6.2	7.6

^aSymmetry of the lowest rovibrational levels.

^bReferences 32, 42, 43.

^cReferences 31, 33.

ports an H geometry for the singlet ground state, in agreement with recent beam scattering experiments.⁶⁰ For the excited state, the observed and calculated R_0 values tend to favor a perpendicular T geometry but as a wide choice of intermediate structures are not presented here, we cannot conclude about the most probable structure for the dimer in its excited state.

B. Vibrational assignment

Our attempts to identify new Q branches corresponding to other subbands remain unsuccessful. Moreover, the preceding rotational analysis have showed that the P and R branches are weaker than expected and therefore even more difficult to detect. Under these conditions, in order to localize the Q branches, we have affected a Lorentzian line shape of 0.5 cm^{-1} width (FWHM) to each measured line with an absorption coefficient above a fixed threshold of $1.2 \times 10^{-8}/\text{cm}$, three times the noise level. The related spectrum is shown in Fig. 10. The labeled peaks correspond to Q branch maxima (ν_Q) and are then red-shifted from the band centers (ν_0). As an example, the Q branch maxima of the previously rotationally analyzed $K=0$ subbands centered at $\nu_0=15813.13$ and 15808.40 cm^{-1} are shifted by -2.1 and -2.0 cm^{-1} , respectively.

Considering the dimer in the semirigid limit in the most stable H geometry, $(\text{O}_2)_2$ has four intermolecular normal modes; ν_1 associated with the intermonomer stretching mode and correlated to $\bar{\omega}_1=23.6\text{ cm}^{-1}$ in quantum calculations of the ground state, ν_2 , associated with the torsion mode ($\Delta\varphi$) (see Fig. 5) and correlated to $\bar{\omega}_2=6.9\text{ cm}^{-1}$, ν_3 and ν_4 associated with the parallel and antiparallel bending ($\bar{\omega}_3, \bar{\omega}_4 > \bar{\omega}_1$).⁴² Again, for symmetry reasons (see Fig. 3 of Ref. 42), only two vibrational modes ν_1 and ν_2 are physically allowed among the lowest vibrational levels involved in the current experimental conditions. As noted before, only the lowest levels of the ground state are significantly populated under our experimental conditions and the strongest Q branch maxima listed in Table VIII and shown in Fig. 10 are expected to arise mostly from the lowest ($K=0$) level of the ground electronic state which is of A_1^+ symmetry and correlated to $(v_1=0, v_2=0)$ in the semirigid limit. The symmetry selection rules imply³⁴ that the upper level of these bands must have a B_1^- symmetry which corresponds to an odd number of vibrational torsion $(v_1'=0, 1, 2, 3, 4, \dots, v_2'=1, 3, 5, 7, \dots)$.^{42,43} Conversely the weaker bands starting from $(K=0)B_1^-$ levels correlated to $(v_1=0, v_2=1)$ have an $(K=1)A_1^+$ upper level correlated to $(v_1'=0, 1, 2, \dots, v_2'=0, 2, 4, \dots)$. The vibrational assignment proposed in Fig. 10 and Table VIII from both intensity and energetic considerations seems to be the most reasonable. The two rotationally analyzed subbands centered at 15813.13 and 15808.40 cm^{-1} are then assigned to $[(v_1'=0, v_2'=1), K'=1]B_1^- \leftarrow [(v_1=0, v_2=0), K=0]A_1^+$ and $[(0,0), 1]A_1^+ \leftarrow [(0,1), 0]B_1^-$ transitions, respectively. Figure 11 displays the energy diagram of the levels of interest in the forthcoming discussion.

The strongest series, $[(v_1', 1), 1]B_1^- \leftarrow [(0,0), 0]A_1^+$, correspond to an excitation of the stretching mode until the dissociation limit. Assuming a constant red-shift of the Q

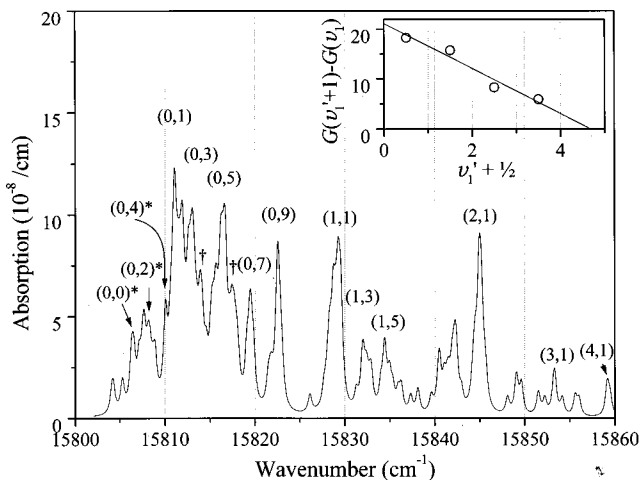


FIG. 10. Broadening of the CW-CRDS spectrum. A Lorentzian line shape of 0.5 cm^{-1} width (FWHM) is affected to each line which absorption coefficient is measured above a fixed threshold of $1.2 \times 10^{-8}/\text{cm}$ in order to emphasize the regions of strong Q lines which characterize the various bands. Most features are assigned to Q branches of subbands corresponding to $[(v_1', v_2'), K'=1]B_1^- \leftarrow [(0,0), 0]A_1^+$ and $[(v_1', v_2'), 1]A_1^+ \leftarrow [(0,1), 0]B_1^-$ transitions. The asterisks (*) are referring to this second transition. The upper state vibrational level is indicated in parentheses (v_1', v_2') . The daggers (\dagger) at 15813.82 and 15817.43 cm^{-1} indicate the subbands centered at 15812.66 and 15818.28 cm^{-1} arising from a $K=2$ level whose upper state is not vibrationally assigned. The insert is a Birge Spomer plot of the differences $G[(v_1'+1), 1]B_1^- - G[(v_1', 1), 1]B_1^-$ with $0 \leq v_1' \leq 3$.

branch maxima compared to the band center, the difference of the upper levels of two successive transitions, $G[(v_1'+1, 1), 1]B_1^- - G[(v_1', 1), 1]B_1^-$, leads to the Birge Spomer plot inserted in Fig. 10, which gives the dissociation energy of $D'_0=49 \pm 4\text{ cm}^{-1}$. The stretching frequency in the upper electronic state can be estimated from $G[(1,1), 1]B_1^- - G[(0,1), 1]B_1^- \cong \bar{\omega}'_1 \cong 18.2 \pm 1.0\text{ cm}^{-1}$. These values are close to those found in Ref. 28 for the excited electronic state $[\text{O}_2(^1\Delta_g)_{v=0} - \text{O}_2(^1\Delta_g)_{v=1}]$: $D'_0=41 \pm 2\text{ cm}^{-1}$ and $\bar{\omega}'_1=17.8 \pm 0.5\text{ cm}^{-1}$ but about twice the theoretical values $D'_0=24\text{ cm}^{-1}$ and $\bar{\omega}'_1=10\text{ cm}^{-1}$.^{33,43}

From the vibrational assignment (see Fig. 10), we infer $G[(0,2), 1]A_1^+ - G[(0,0), 1]A_1^+ \cong 2\bar{\omega}'_2=1.7\text{ cm}^{-1}$ and $G[(1,3), 1]B_1^- - G[(1,1), 1]B_1^- = 2.7\text{ cm}^{-1}$ not far from the theoretical values of 1.1 and 1.9 cm^{-1} , respectively.⁴³ The difference between the experimental and theoretical values

TABLE VIII. Observed Q branch maxima (ν_Q) of the $[(v_1', v_2'), K'=1]B_1^- \leftarrow [(0,0), K=0]A_1^+$ and $[(v_1', v_2'), 1]A_1^+ \leftarrow [(0,1), 0]B_1^-$ subbands.

$v_2' \setminus v_1'$		0	1	2	3	4
1	$B_1^- \leftarrow A_1^+$	15 811.04	15 829.28	15 844.99	15 853.27	15 859.18
3		15 812.99	15 832.01			
5		15 816.55	15 834.40			
7		15 819.46				
9		15 822.53				
0	$A_1^+ \leftarrow B_1^-$	15 806.40				
2		15 808.16				
4		15 810.06				

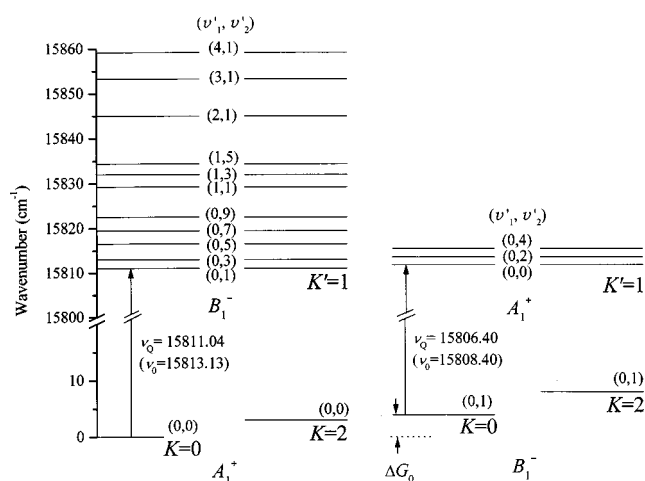


FIG. 11. Energy levels in the ground $[\text{O}_2(^3\Sigma_g^-)_{v=0}]_2$ and excited $[\text{O}_2(^1\Delta_g)_{v=0}]_2$ electronic singlet states of the $(\text{O}_2)_2$ dimer. The energy of the $K=0$ level of B_1^- symmetry was obtained from the determination of ΔG_0 , whereas the upper levels energy are those of the Q branch maxima (ν_Q) and are then red-shifted from their origins (ν_0). The $K=2$ levels positions are placed arbitrarily.

may result from an underestimation of the well depth of the excited state semiempirical potential.⁴³ Nevertheless, we are aware that our experimental values cannot be sustained by a rotational analysis in reason of perturbations that could shift our determined band heads.

We can infer now the separation between the lower levels of the two rotationally analyzed subbands with $K=0$, namely, $[(0,0),0]A_1^+$ and $[(0,1),0]B_1^-$. As both upper levels correspond to $K=1$ and as the rotational constants are close for both excited states, we have then (see Fig. 11)

$$\begin{aligned} \Delta G_0(B_1^- - A_1^+) &= \tilde{\omega}_2 = G[(0,1),0]B_1^- - G[(0,0),0]A_1^+ \quad (10) \\ &= 15\,813.13 - 15\,808.40 \\ &\quad + \{G'[(0,1),1]B_1^- - G'[(0,0),1]A_1^+\}. \end{aligned}$$

The second term corresponds to $\tilde{\omega}'_2$, estimated to be 0.85 cm^{-1} just above, and the + sign before this term comes from the fact that the lowest ($K=1$) B_1^- excited state is lower in energy than the lowest ($K=1$) A_1^+ excited level (see Fig. 1 of Ref. 43). We then estimate the value of the torsion mode

ν_2 to be about 5.58 cm^{-1} in good agreement with the predicted value (6.9 cm^{-1}). The related Boltzmann factor at $T=12\text{ K}$ is then $\exp(-5.58/kT)=0.511$ leading to a ratio of 1.96 between the intensity of the lines of the two subbands instead of the measured value of 2.3. As the rotational temperature is very close for both subbands, we conclude that the transition moment is slightly higher for $B_1^- \leftarrow A_1^+$ than for $A_1^+ \leftarrow B_1^-$, except if a non-Boltzmann equilibrium between the A_1^+ and B_1^- levels occurs in the cooling of the jet expansion.

The subband arising from the lowest $K=2$ level does not allow an estimation of the separation between the origins of $K=2$ and $K=0$ levels of A_1^+ or B_1^- symmetry in the ground state because of the nonassignment of the excited $K'=1$ vibrational level. Nevertheless from the above intensity considerations we can estimate the separation $\Delta G_2(B_1^- - A_1^+)$ and $\Delta G_0(B_1^- - A_1^+)$ for $K=2$ and $K=0$ levels in the ground state. From the average intensity of the Q branches given in Table VI, we have $\exp(-\Delta G_2/kT)=1.10/2.34$ and $\exp(-\Delta G_0/kT)=1.9/4.36$ which gives $\Delta G_2=6.3\text{ cm}^{-1}$ and $\Delta G_0=6.9\text{ cm}^{-1}$ in good agreement with the above determination of ΔG_0 and with predicted values.⁴²

V. CONCLUSION

The high sensitivity and resolution of the CW-CRDS technique has allowed the first rotational analysis of a transition of the $(\text{O}_2)_2$ open-shell complex and the first experimental determination of its structure. A tentative vibrational assignment has been also given. As previously predicted, $(\text{O}_2)_2$ is a typical van der Waals system between normal rigid molecules and special van der Waals dimers with free internal rotations such as $(\text{H}_2)_2$, rare gas- H_2 or $\text{CO}-\text{H}_2$. In spite of its shallow potential well, it has a large number of bound rotational and vibrational states though only levels of A_1^+ or B_1^- symmetry are populated due to zero nuclear spin of the oxygen atom. The theoretical calculations were of great help in disentangling the lines of the analyzed subbands. The spectroscopic parameters obtained here corroborate the H geometry of the ground singlet state of the O_2 dimer and they confirm the floppy structure of $(\text{O}_2)_2$ in its excited state. We have gathered in Table IX the main results of the present paper. We also give for comparison the theo-

TABLE IX. Summary of the main experimental results and comparison with theoretical results.

	$[\text{O}_2(^3\Sigma_g^-)_{v=0}]_2$		$[\text{O}_2(^1\Delta_g)_{v=0}]_2$	
	Expt ^a	Calc ^b	Expt ^a	Calc ^c
Dimer geometry	H		H, X, T	
Intermonomer distance $R_0(a_0)$	6.04–6.14 ^a	6.44–6.51	7.50–7.53	7.72–7.75
Dissociation energy $D_0(\text{cm}^{-1})$	65 ± 15^d	74	49 ± 4	24
Stretching mode $\tilde{\omega}_1(\text{cm}^{-1})$	23.8 ± 0.5^e	23.6	18.2 ± 1.0	10
Torsion mode $\tilde{\omega}_2(\text{cm}^{-1})$	$\approx 5.6^a$	6.9	≈ 0.85	0.55

^aThis work.

^bReference 42.

^cReference 43.

^dReference 6.

^eReference 28.

retical values determined in Refs. 42 and 43. Nevertheless, substantial work remains to be done in order to confirm and complete the present analysis for both states.

In the short term, the determined rotational constants of the ground state should allow to tackle the analysis of the much more congested (1–0) spectrum previously recorded at 578 nm by ICLAS.⁶

From an experimental point of view, a lower temperature of the jet (He seeded jet for example) would simplify the present (0–0) spectrum and improve the detection of the first lines of every branch which are of primary importance to assign a transition. This will be of great help to confirm and improve the knowledge of the ground state.

In addition, in the mid-infrared, widely tunable quantum-cascade distributed-feedback lasers capable of emitting tens to hundreds of milliwatts with linewidths of the order of tens of MHz are very promising for CRDS.⁶¹ In spectroscopic applications, these lasers could operate pulsed at room temperature or in cw mode at cryogenic temperatures.⁶² This should allow to probe the first transition of the O₂ dimer at 6.4 μm, corresponding to a stretching excitation of one of the monomers.

In the midterm, we hope that the present data will help to refine the potential energy surface of (O₂)₂, which is tightly linked with thermophysical properties of strong atmospheric interest and that our experiments will allow us to clearly define the (O₂)₂ atmospheric absorption spectra.

ACKNOWLEDGMENTS

We are indebted to A. Bouvier (Lyon) for computing assistance in the fitting procedure. We would like to thank V. Veyret (Berlin) for discussion, A. Ross for critical reading of the manuscript, and S. Churassy (Lyon) for his continuous interest. We warmly thank A. A. Vigasin for having communicated his results on the calcul of the dimer concentration in the jet prior to publication. Partial financial support from the PNCA (No. 99N51/0208) is acknowledged.

- ¹T. E. Gough, R. E. Miller, and G. Scoles, *J. Phys. Chem.* **85**, 4041 (1981).
- ²R. E. Miller and R. O. Watts, *Chem. Phys. Lett.* **105**, 409 (1984).
- ³M. A. Walsh, T. H. England, T. R. Dyke, and B. J. Howard, *Chem. Phys. Lett.* **142**, 265 (1987).
- ⁴D. F. Coker, R. E. Miller, and R. O. Watts, *J. Chem. Phys.* **82**, 3554 (1985).
- ⁵J. B. Paul, C. P. Collier, R. J. Saykally, J. J. Scherer, and A. O'Keefe, *J. Phys. Chem.* **101**, 5211 (1997).
- ⁶A. Campargue, L. Biennier, A. Kachanov, R. Jost, B. Bussery-Honvault, V. Veyret, S. Churassy, and R. Bacis, *Chem. Phys. Lett.* **288**, 734 (1998).
- ⁷R. L. Miller, A. G. Suits, P. L. Houston, R. Toumi, J. A. Mack, and A. M. Wodkte, *Science* **265**, 1831 (1994).
- ⁸A. J. C. Varandas and W. Wang, *Chem. Phys.* **215**, 167 (1997).
- ⁹D. Lauvergnat and D. C. Clary, *J. Chem. Phys.* **108**, 3566 (1998).
- ¹⁰T. G. Slanger, *Science* **265**, 1817 (1994).
- ¹¹P. J. Crutzen, J. V. Grooß, C. Brühl, R. Müller, and J. M. Russell, *Science* **268**, 705 (1995).
- ¹²J. A. Syage, *J. Phys. Chem.* **99**, 16530 (1995).
- ¹³C. A. Rogaski, J. A. Mack, and A. M. Wodkte, *Faraday Discuss.* **100**, 229 (1995).
- ¹⁴C. A. Rogaski, J. A. Mack, and A. M. Wodkte, *J. Chem. Phys.* **104**, 775 (1996).
- ¹⁵R. T. Jongma, S. Shi, and A. M. Wodkte, *J. Chem. Phys.* **111**, 2588 (1999).
- ¹⁶D. Perner and U. Platt, *Geophys. Res. Lett.* **7**, 1053 (1980).
- ¹⁷W. M. Calvin and J. R. Spencer, *Icarus* **130**, 505 (1997).
- ¹⁸S. Yoshida, K. Shimizu, T. Sawano, T. Tokuda, and T. Fujioka, *Appl. Phys. Lett.* **54**, 2400 (1989).
- ¹⁹*Singlet O₂*, edited by A. A. Frimer (CRCR, Boca Raton, Florida, 1985), Vol. I.
- ²⁰D. Ritz, M. Haussman, and U. Platt, *SPIE* **1715**, 200 (1992).
- ²¹C. Hermans, A. C. Vandaele, M. Van Roozendaele, P. C. Simon, M. Carleer, S. Fally, R. Colin, B. Copquart, A. Jenouvrier, and M. F. Mérienne, in *Proceedings of the Atmospheric Spectroscopy and Applications Workshop* (G.S.M.A., Université de Reims Champagne, Reims, 1996), p. 83.
- ²²A. A. Vigasin and Z. Slanina, *Molecular Complexes in the Earth's, Planetary, Cometary, and Interstellar Atmospheres* (World Scientific, Singapore, 1998).
- ²³F. Thibault, V. Menoux, X. Le Doucen, and J. M. Hartmann, *Appl. Opt.* **36**, 563 (1997).
- ²⁴G. Moreau, J. Boisssoles, C. Boulet, R. Tipping, and Q. Ma, *J. Quant. Spectrosc. Radiat. Transfer* (in press).
- ²⁵H. M. Bevssek, M. Ahmed, D. S. Peterka, F. C. Scales, and A. G. Suits, *Faraday Discuss.* **108**, 131 (1998).
- ²⁶D. S. Peterka, M. Ahmed, A. G. Suits, K. J. Wilson, A. Korlein, M. Nooijen, and R. J. Barthelet, *J. Chem. Phys.* **110**, 6095 (1999).
- ²⁷O. L. J. Gijzeman, E. A. Ogryzlo, and R. P. H. Rettschnick, *J. Chem. Phys.* **52**, 3718 (1970).
- ²⁸C. A. Long and G. E. Ewing, *J. Chem. Phys.* **58**, 4824 (1973).
- ²⁹J. Goodman and L. E. Brus, *J. Chem. Phys.* **67**, 4398 (1977).
- ³⁰D. E. Stogryn and J. O. Hirschfelder, *J. Chem. Phys.* **31**, 1531 (1959).
- ³¹B. Bussery and P. E. S. Wormer, *J. Chem. Phys.* **99**, 1230 (1993).
- ³²V. Veyret, Ph.D. thesis, Université Lyon I, France, 1998 (unpublished).
- ³³B. Bussery, *Chem. Phys.* **184**, 29 (1994).
- ³⁴B. Bussery and V. Veyret, *J. Chem. Phys.* **108**, 3243 (1998).
- ³⁵M. D. Wheeler, S. M. Newmann, A. J. Orr-Ewing, and M. N. R. Ashfold, *J. Chem. Soc., Faraday Trans.* **94**, 337 (1998).
- ³⁶S. Cheskis, I. Derzy, V. A. Lozovsky, A. Kachanov, and D. Romanini, *Appl. Phys. B: Lasers Opt.* **66**, 377 (1998).
- ³⁷X. Mercier, P. Jamette, J. F. Pauwels, and P. Desgroux, *Chem. Phys. Lett.* **305**, 334 (1999).
- ³⁸D. Romanini, L. Biennier, F. Salama, A. Kachanov, L. J. Allamandola, and F. Stoeckel, *Chem. Phys. Lett.* **303**, 165 (1999).
- ³⁹D. Romanini, A. A. Kachanov, and F. Stoeckel, *Chem. Phys. Lett.* **270**, 538 (1997).
- ⁴⁰D. Romanini, P. Dupré, and R. Jost, *Vib. Spectrosc.* **19**, 93 (1999).
- ⁴¹D. Romanini, A. A. Kachanov, and F. Stoeckel, *Chem. Phys. Lett.* **270**, 546 (1997).
- ⁴²B. Bussery-Honvault and V. Veyret, *Phys. Chem. Chem Phys.* **1**, 3387 (1999).
- ⁴³V. Veyret, B. Bussery-Honvault, and S. Ya Umanskii, *Phys. Chem. Chem Phys.* **1**, 3395 (1999).
- ⁴⁴A. O'Keefe and D. A. G. Deacon, *Rev. Sci. Instrum.* **59**, 2544 (1988).
- ⁴⁵D. J. Nesbitt, *Chem. Rev.* **88**, 843 (1988).
- ⁴⁶A. Savitzky and M. J. E. Golay, *Anal. Chem.* **36**, 1627 (1964).
- ⁴⁷S. Gerstenkorn and P. Luc, *Atlas de la Molécule d'iode* (Editions du CNRS, Paris, 1978).
- ⁴⁸S. Gerstenkorn and P. Luc, *Rev. Phys. Appl.* **8**, 791 (1979).
- ⁴⁹H. D. Babcock and L. Herzberg, *Astrophys. J.* **108**, 167 (1948).
- ⁵⁰A. A. Vigasin, *Chem. Phys. Lett.* **290**, 495 (1998).
- ⁵¹A. Vigasin (private communication, 1999).
- ⁵²A. Kachanov and T. V. Plakhotnik, *Opt. Commun.* **47**, 257 (1983).
- ⁵³R. Georges, A. Delon, F. Bylicki, R. Jost, A. Campargue, A. Charvat, M. Chenevier, and F. Stoeckel, *Chem. Phys.* **190**, 207 (1995).
- ⁵⁴B. F. Minaev, *Russ. J. Phys. Chem.* **68**, 1300 (1994).
- ⁵⁵B. F. Minaev, V. D. Nikolaev, and H. Ågren, *Spectrosc. Lett.* **29**, 677 (1996).
- ⁵⁶G. Herzberg, *Molecular Spectra and Molecular Structure III. Electronic Spectra and Electronic Structure of Polyatomic Molecules* (Van Nostrand, New York, 1966).
- ⁵⁷P. R. Bunker, *Molecular Symmetry and Spectroscopy* (Academic, New York, 1979).
- ⁵⁸A. R. W. McKellar, *Chem. Phys. Lett.* **186**, 58 (1991).

⁵⁹C. Amiot and J. Vergés, *Can. J. Phys.* **59**, 1391 (1981).

⁶⁰V. Aquilanti, D. Ascenzi, M. Bartolomei, D. Cappelletti, S. Cavalli, M. de Castro Vítors, and F. Pirani, *Phys. Rev. Lett.* **82**, 69 (1999).

⁶¹C. Gmachl, F. Capasso, J. Faist, A. Hutchinson, A. Tredicucci, D. Sivco,

J. N. Baillargeon, S. Chu, and A. Y. Cho, *Appl. Phys. Lett.* **72**, 1430 (1998).

⁶²S. W. Sharpe, J. F. Kelly, J. S. Hartman, C. Gmachl, F. Capasso, D. Sivco, J. N. Baillargeon, and A. Y. Cho, *Opt. Lett.* **23**, 1396 (1998).